scientific reports

OPEN

Paper-based broadband flexible photodetectors with van der Waals materials

Erfan Mahmoodi[1], Morteza Hassanpour Amiri[2], Abdollah Salimi[3,4], Riccardo Frisenda[5], Eduardo Flores[6], José R. Ares[7], Isabel J. Ferrer[7,8], Andres Castellanos-Gomez[5] & Foad Ghasemi[1]✉

Layered metal chalcogenide materials are exceptionally appealing in optoelectronic devices thanks to their extraordinary optical properties. Recently, their application as flexible and wearable photodetectors have received a lot of attention. Herein, broadband and high-performance paper-based PDs were established in a very facile and inexpensive method by rubbing molybdenum disulfide and titanium trisulfide crystals on papers. Transferred layers were characterized by SEM, EDX mapping, and Raman analyses, and their optoelectronic properties were evaluated in a wavelength range of 405–810 nm. Although the highest and lowest photoresponsivities were respectively measured for TiS_3 (1.50 mA/W) and MoS_2 (1.13 μA/W) PDs, the TiS_3–MoS_2 heterostructure not only had a significant photoresponsivity but also showed the highest on/off ratio (1.82) and fast response time (0.96 s) compared with two other PDs. This advantage is due to the band offset formation at the heterojunction, which efficiently separates the photogenerated electron–hole pairs within the heterostructure. Numerical simulation of the introduced PDs also confirmed the superiority of TiS_3–MoS_2 heterostructure over the other two PDs and exhibited a good agreement with the experimental results. Finally, MoS_2 PD demonstrated very high flexibility under applied strain, but TiS_3 based PDs suffered from its fragility and experience a remarkable drain current reduction at strain larger than ± 0.33%. However, at lower strains, all PDs displayed acceptable performances.

With the development of smart and Internet of Things (IoT) based technologies, great efforts have been made on wearable and flexible electronic devices which are mostly implemented on Polyethylene terephthalate (PET) and Polydimethylsiloxane (PDMS) substrates[1]. However, in addition to high manufacturing costs and lack of biodegradability, their fabrication processes require advanced laboratory equipment, which obstruct their possible practical applications[2]. Flexible paper-based electronic devices are a new class of high-performance devices that offer admirable properties with facile and low-cost fabrication processes, ending in lightweight and environmentally friendly devices that are very promising for the future of smart electronics[3–5]. Flexible photodetectors (PDs), as a member of this family, have received a great deal of attention, suitable for optoelectronic systems such as optical communications, environmental monitoring, and imaging[6].

Two-dimensional (2D) materials, especially the chalcogenides family, have been increasingly used in optoelectronic devices in recent years due to their adjustable band gap, high electrical conductivity, and effective light-matter interactions[7]. Metal chalcogenide based PDs have shown high photoresponsivity, fast response time, and high quantum efficiency[8]. Interestingly, their paper-based PDs also demonstrates such a high performance[9–11]. Sahatiya et al. fabricated a MoS_2-Carbon Quantum dot (CQDs) based PD on cellulose paper using a hydrothermal growth of MoS_2 and casting of CQDs[12]. Their reported device showed a photoresponsivity of 18 mA/W in the visible region with a response time of ~ 0.57 s. Selamneni et al. hydrothermally grown MoS_2 on cellulose

[1]Nanoscale Physics Device Lab (NPDL), Department of Physics, University of Kurdistan, Sanandaj 66177-15175, Iran. [2]School of Electrical and Computer Engineering, University of Tehran, Tehran 14395-515, Iran. [3]Department of Chemistry, University of Kurdistan, Sanandaj 66177-15175, Iran. [4]Research Center for Nanotechnology, University of Kurdistan, Sanandaj 66177-15175, Iran. [5]Materials Science Factory, Instituto de Ciencia de Materiales de Madrid (ICMM-CSIC), Madrid 28049, Spain. [6]Centro de Nanociencias y Nanotecnología (CNyN), Universidad Nacional Autónoma de México (UNAM), Ensenada, Baja California 22860, México. [7]Materials of Interest in Renewable Energies Group (MIRE Group), Departamento de Física de Materiales, Universidad Autónoma de Madrid, UAM, Madrid 28049, Spain. [8]Instituto Nicolás Cabrera, Universidad Autónoma de Madrid, UAM, Spain. ✉email: f.ghasemi@uok.ac.ir

1

paper followed by decorating with various metal nanoparticles (Au, Pt, and Pd)[11]. The photoresponsivities and response times of the PDs were measured to be around 45–100 mA/W and 0.9–1.2 s in the visible range, respectively. Cordeiro et al. introduced near-infrared PDs by growing MoS_2 on cellulose paper using a hydrothermal technique. Their PD showed a photoresponsivity of about 200 mA/W and a response time of 3.7 s[13]. However, majority of methods used for the fabrication of paper-based PDs are time-consuming, complex, and consisting wet procedures. In contrast, rubbing of bulk crystal on ordinary paper can be a potential alternative to facile realization of paper-based PDs through a simple, fast and completely dry process. As an example, Mazaheri et al. transferred MoS_2 flakes by rubbing the corresponding crystal on paper and reported a paper based PD with a photoresponsivity of 1.5 µA/W in a wavelength range of 365 to 940 nm[14].

In this work, MoS_2 and TiS_3 bulk crystals were employed to fabricate paper-based PDs by transferring their corresponding flakes through finger-rubbing process. TiS_3 is another class of 2D materials with MX_3 structure, which its unique properties make it very suitable for optoelectronic applications[15]. TiS_3 is an n-type semiconductor with a direct band gap of 1.1 eV independent of thickness with high reported electron mobility and photoresponsivity[16]. Unlike MX_2, it has a chain-like structure that provides large aspect ratios with better electrical connectivity even in lower loading fractions[16]. In addition, the electronic band structure of TiS_3 could be matched with MoS_2 to provide a suitable heterostructure for optoelectronic applications. Accordingly, three types of MoS_2, TiS_3, and TiS_3–MoS_2 PDs were fabricated and their optoelectronic properties were carefully evaluated in the wavelength range of 405 to 810 nm. Based on the results, the highest photoresponsivity were measured for TiS_3 PDs and the lowest for MoS_2 PDs. In the case of TiS_3–MoS_2 (MoS_2 film was placed on top of the TiS_3 film and exposed to light), it exhibited a faster response time, and higher on–off ratio thanks to formation of band offset at semiconductor heterojunctions. Numerical simulations also confirmed the superiority of TiS_3–MoS_2 PDs over MoS_2 PDs. Moreover, to evaluate the flexible performance of the PDs, the introduced devices were bent on both positive and negative curvatures and their I_{ds}–V_{ds} and photocurrent characteristics were measured under strain range of ± 0.27 to ± 0.54%. The results showed that MoS_2 PDs had high flexibility, but TiS_3 based PDs were associated with the decline of drain current and photodetection responsivity at applied strains larger than ± 0.33%.

Results and discussions

SEM image and XRD analysis of the grown TiS_3 microcrystals are presented in Fig. S1. Before transferring the flakes, the surface of paper was investigated by SEM and EDX measurements. As can be seen in Fig. S2a, the paper is formed by stacked cellulose fibers and it presents deep gaps/voids between fibers. EDX analysis also confirms the presence of carbon (C), oxygen (O), calcium (Ca), silicon (Si), aluminum (Al), iron (Fe), sodium (Na), and manganese (Mg) in the raw paper where their atomic percentages are listed in the inset of Fig. S2b.

Figure 1 shows the characterization of the deposited flakes on paper substrates. The schematic illustration of the TiS_3–MoS_2 heterostructure and its corresponding photograph are also presented in panels (a) and (b) of Fig. 1, respectively. Figure 1c exhibits the SEM image of the MoS_2 flakes on the paper. According to the figure, MoS_2 flakes cover the fibers and gaps between fibers of the paper. The deposited TiS_3 flakes are also presented in Fig. 1d in which the thickness of the film is measured to be ~ 10 µm. Moreover, the SEM image of the TiS_3–MoS_2 heterostructure is observed in Fig. 1e. Due to softness and flexibility of MoS_2, it forms a smoother film than TiS_3 on paper, which is visible in Fig. 1e. The EDX analysis of MoS_2, TiS_3, and TiS_3–MoS_2 samples on papers is presented in Fig. 1f,g. By rubbing MoS_2 on the paper, the Mo and S elements becomes significant (Fig. 1f). The EDX analysis of TiS_3 sample also proves the presence of S and Ti elements according to Fig. 1g. SEM–EDX analysis of transferred TiS_3 flakes is also presented in Fig. S3. In the case of TiS_3–MoS_2 film, dominant elements are S, Mo, and Ti (Fig. 1h). The C, O and Ca elements come from raw paper. Table S1 summarizes the element contents of all samples with their weight and atomic percentages.

Figure 2a exhibits the magnified SEM image of the TiS_3–MoS_2 film where the MoS_2 film is deposited on the TiS_3 film. However, some TiS_3 microcrystals may also appear on top of the film due to the rubbing process. The Raman spectra of MoS_2, TiS_3, and TiS_3-MoS_2 samples are also presented in Fig. 2b. For MoS_2, E^1_{2g} and A_{1g} peaks are found at 379 and 403 cm^{-1}, respectively[17]. In the case of TiS_3, the 193, 385 and 627 cm^{-1} peaks refer to A_g and E_g modes, respectively[18]. There is also one additional peak located at 507 cm^{-1}, which refers to B_{1g} peak of TiO_2[19]. This oxide peak may have appeared during the growth of TiS_3 microcrystals in the ampoule process. The Raman spectrum of TiS_3–MoS_2 sample contains all peaks of both structures. The corresponding A_g, E^1_{2g}, and A_{1g} peaks of TiS_3 and MoS_2 are also fitted in the Raman spectrum of the hybrid sample. Figure 2c shows the mapping analysis of the TiS_3–MoS_2 sample where the dominant elements are separately shown in Fig. 2d. Accordingly, O, C, and Ca elements are due to the raw paper, and elements of Ti, Mo, and S originate from the TiS_3 and MoS_2 films. It can be seen that all elements are uniformly distributed on the paper.

To investigate the optoelectronic properties of the films, MoS_2, TiS_3, and TiS_3-MoS_2 PDs were fabricated. Details of their fabrication are provided in the experimental section. The fabrication steps of MoS_2 and TiS_3 PDs are shown in Figs. S4 and S5, respectively. In the case of TiS_3–MoS_2 PD, the fabrication steps are presented in Fig. 3.

Panels (a) to (c) of Fig. 4 display I–V characteristics of the MoS_2, TiS_3, and TiS_3–MoS_2 PDs at a bias range of − 10 to + 10 V in dark and under 532 nm laser illumination at different power intensities. In all three PDs, significant photocurrents were generated compared to the dark state. The incident power is normalized in terms of laser spot and PD's channel areas. Accordingly, the effective incident power is calculated as:

$$P_{eff} = P_{laser} \times A_{device}/A_{laser} \qquad (1)$$

where P_{laser} is the power of the laser, A_{device} is the area of the PD's channel, and A_{laser} is the area of the laser spot. The diameter of the 532 nm laser spot was 2.81 mm and its area (A_{laser}) was measured to be 6.22 mm^2. As the laser intensity increases, the photocurrent also increases for all three PDs. In detail, the drain currents were measured
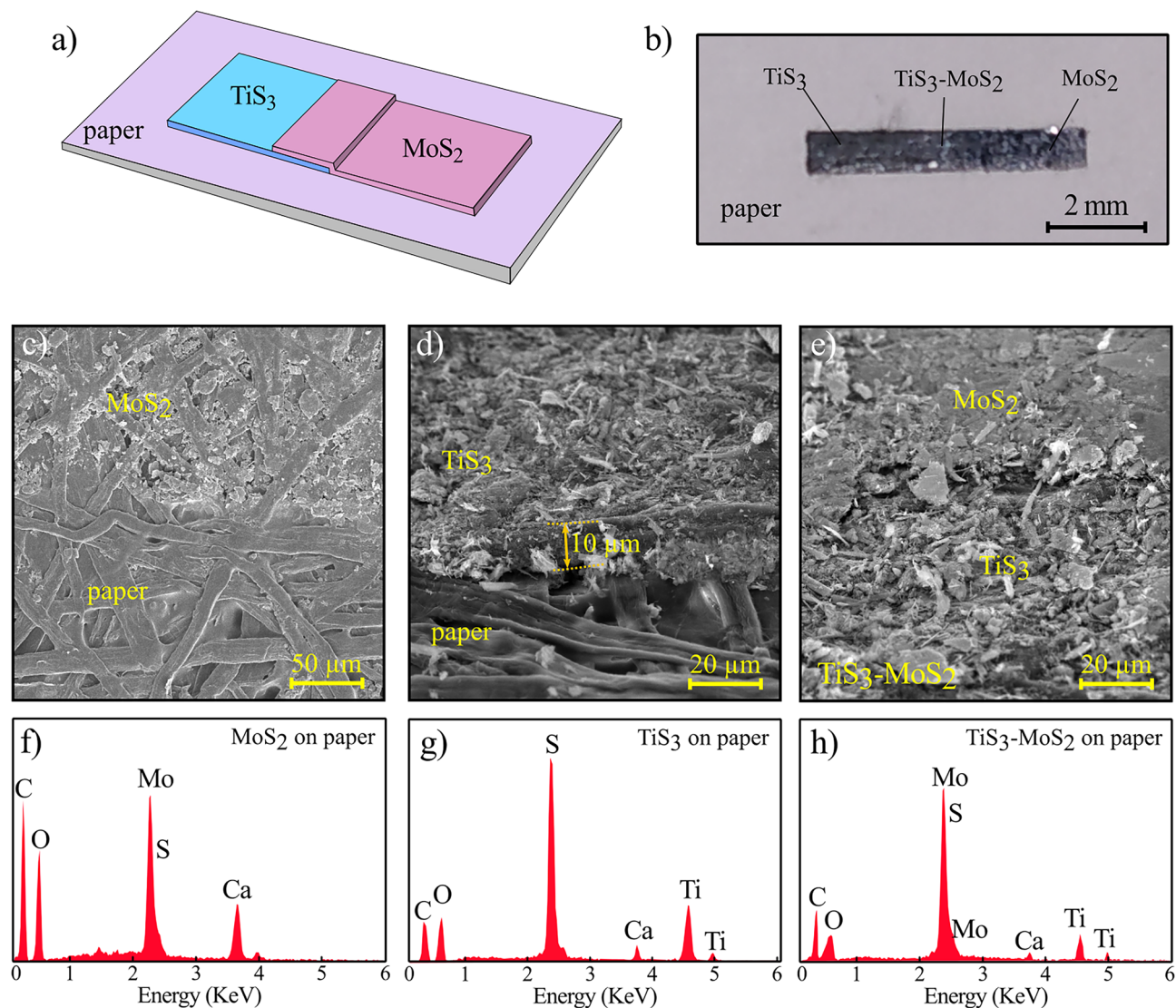
Figure 1. (a) Schematic illustration of the TiS$_3$-MoS$_2$ film on the paper. (b) Photograph of the fabricated TiS$_3$-MoS$_2$ film on the paper. SEM image of the transferred (c) MoS$_2$, (d) TiS$_3$, (e) TiS$_3$-MoS$_2$ flakes on the paper. EDX analysis of the (f) MoS$_2$, (g) TiS$_3$, and (h) TiS$_3$-MoS$_2$ films on the paper.

in the range of ~ 0–4 nA, ~ 0–8 μA and ~ 0–450 nA for MoS$_2$, TiS$_3$, and TiS$_3$–MoS$_2$ PDs at a biasing voltage of 0–10 V, respectively. Interestingly, the I$_{ds}$ in TiS$_3$–MoS$_2$ is significantly higher than that of individual MoS$_2$, which indicates the effective role of the band offset formation in increasing the photocurrent. The I–V curves of the all PDs in response to 405, 655, and 810 nm laser illuminations are also shown in Fig. S6 where all PDs respond to the laser irradiation by an increase in current. Figure 4d–i compare the photocurrent and photoresponsivity of all three PDs at different power intensities of 532 nm at an applied voltage of 10 V. According to Fig. 4d–f, with increasing effective incident power (from zero to a few mW), increase in the photocurrents are occurred. In the MoS$_2$ PD, the photocurrent increases to about 1.6 nA. For TiS$_3$, this value is more noticeable and a 1.0 μA increase of photocurrent is observed. In the case of TiS$_3$-MoS$_2$ PD, photocurrent increases up to 300 nA. The photoresponsivity of the PDs are calculated based on the following equation[20]:

$$R = I_{ph}/P_{eff} \qquad (2)$$

where I$_{ph}$ is the photocurrent of the PDs. In the MoS$_2$ PD, increasing the effective power associates with decrease of the photoresponsivity. The same trends are also observed for TiS$_3$, and TiS$_3$–MoS$_2$ PDs. As the incident power increases, more photocarriers are generated, which increases the recombination rate of photogenerated carriers or the possibility of being captured by the traps, leading to a decrease in R[21,22]. In general, the photoresponsivities are measured in the range of 0.4–1.2 μA/W, 0.4–1.6 mA/W, and 90–170 μA/W for MoS$_2$, TiS$_3$, and TiS$_3$–MoS$_2$ PDs, respectively. Accordingly, the photoresponsivity of the last two PDs is three and two orders of magnitude greater than that of MoS$_2$ PD.

Figure 5a–c show the measured photocurrent in terms of the different effective powers of the 532 nm laser. Accordingly, an increase in the optical powers leads to an increase in photocurrent in all PDs. Panels (d) to (f)
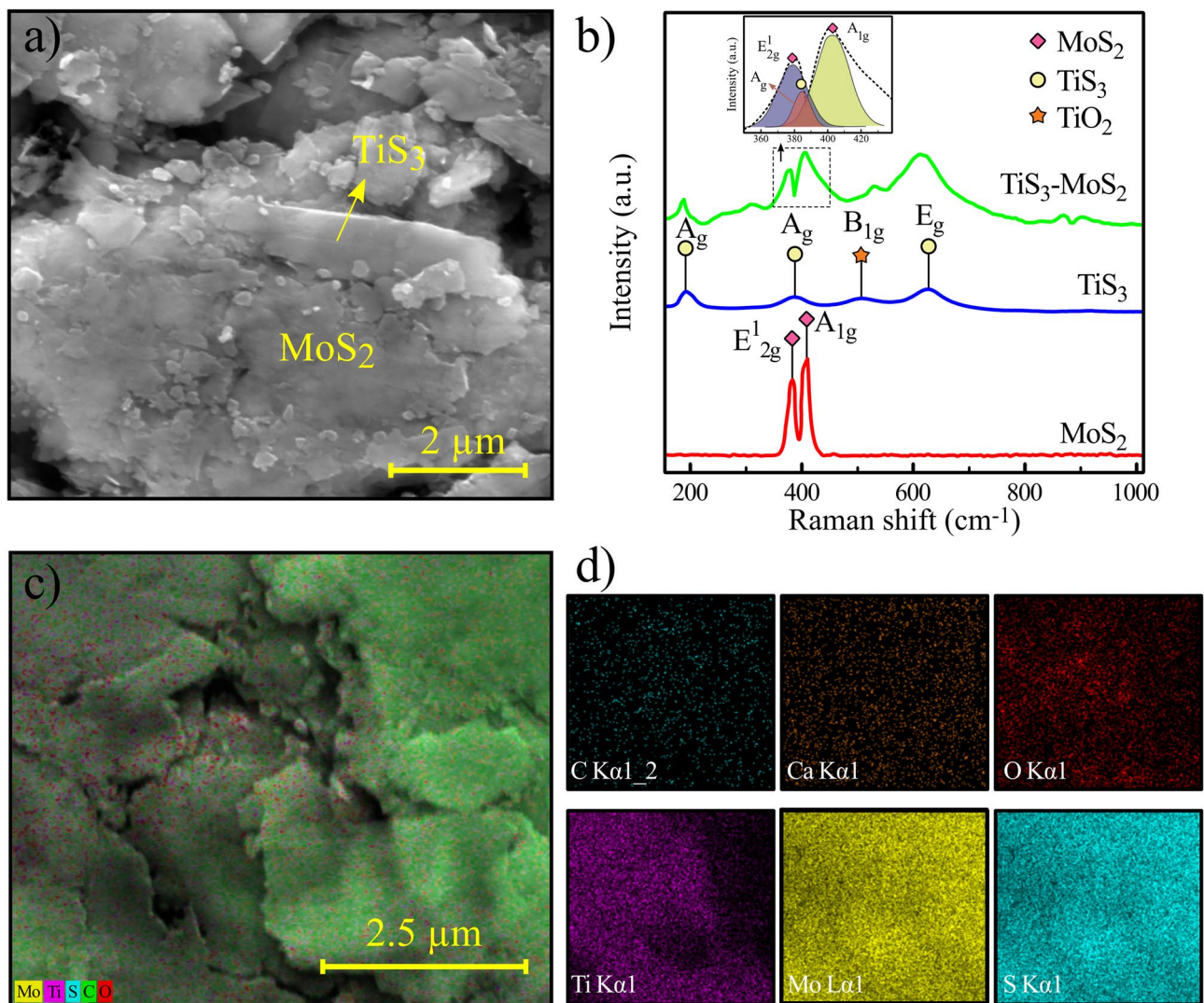
Figure 2. Characterization of the TiS_3-MoS_2 film on the paper. (**a**) SEM image of the film. (**b**) Raman spectra of the MoS_2, TiS_3, and TiS_3-MoS_2 films. (**c**) Mapping analysis of the TiS_3-MoS_2 sample on the paper. d) Elemental mapping of six dominant elements in the TiS_3-MoS_2 sample.
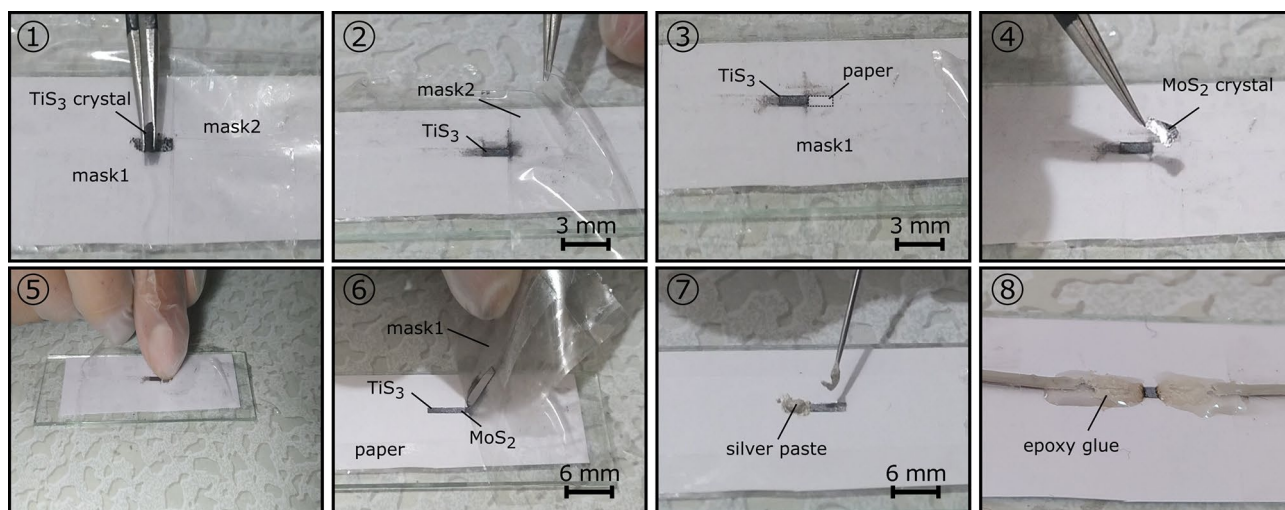
**Figure 3.** Fabrication steps of the TiS_3-MoS_2 PD.
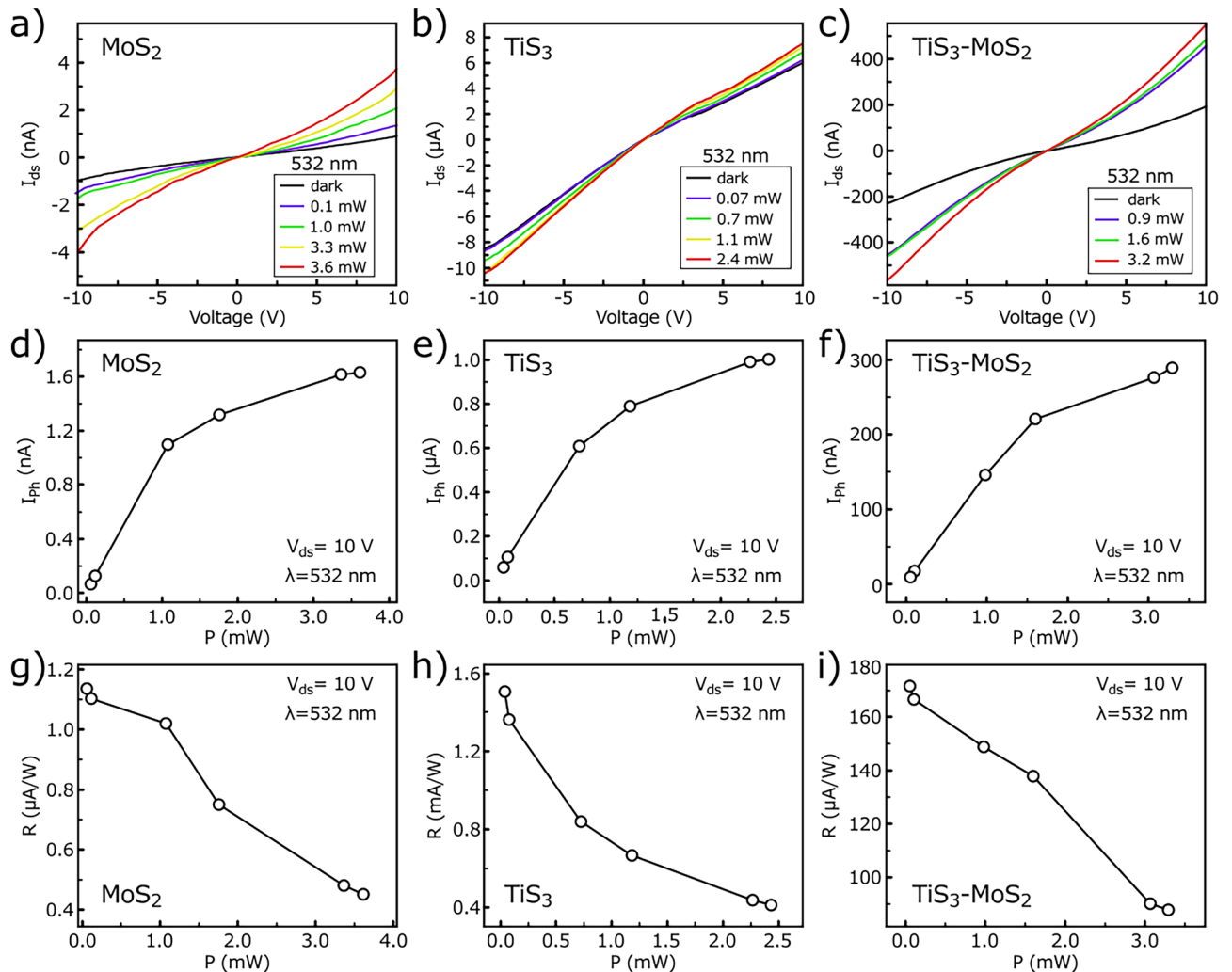
Figure 4. I-V characteristics of the (**a**) MoS_2, (**b**) TiS_3, and (**c**) TiS_3-MoS_2 PDs under 532 nm laser illumination at different power intensities. Photocurrent versus incident power intensity for (**d**) MoS_2, (**e**) TiS_3, and (**f**) TiS_3-MoS_2 PDs under 532 nm laser illumination at an applied voltage of 10 V. Photoresponsivity versus incident power intensity for (**g**) MoS_2, (**h**) TiS_3, and **i**) TiS_3-MoS_2 PDs under 532 nm laser illumination at a supply voltage of 10 V.

of Fig. 5 display the time trace response of the PDs to 532 nm laser illumination at a drain voltage of 10 V at an incident power of 10 mW. Rise time (τ_{on}) is defined as the time taken to increase the current from 10 to 90% of its baseline under laser illumination[23]. The fall time (τ_{off}) is the time required to reduce the current from 90 to 10% of its baseline[24]. For MoS_2, the rise and fall times are measured to be 2.17 and 9.99 s, respectively. In the TiS_3 PD, the τ_{on} and τ_{off} of 2.4 and 17.44 s are measured and in the TiS_3–MoS_2 PD, τ_{on} and τ_{off} of about 0.96 and 8.42 s are calculated that it shows faster switching performance compared with two other PDs. In the hybrid PD, MoS_2 is at the top and is more exposed to light, so the final behavior of the hybrid is more tended toward MoS_2 than TiS_3. For this reason, its photoresponsivity is associated with improvement compared with the MoS_2 PD due to the formation of band offset and efficient charge separation. Moreover, the channel length of TiS_3 is about 1 mm in the hybrid PD, which is half that of individual TiS_3 PD. Hence, the needle-like TiS_3 flake has lower series resistance and therefore shows a faster response time[25,26]. Furthermore, due to the growth process, TiS_3 probably has more defects than MoS_2, so it has a slower response time[27]. However, some part of the TiS_3 is buried under (passivated by) MoS_2 in the hybrid PD and is resulted in less ambient gas absorption, which speeds up the response time[27].

Figure 6a compares the photoresponsivity of several fabricated PDs at an applied voltage of 10 V under a laser wavelength of 532 nm. It is observed that all three TiS_3 PDs have the highest photoresponsivity, followed by TiS_3–MoS_2 and MoS_2 samples, respectively. In general, the R are measured in the range of 0.67–1.56 mA/W for TiS_3 PDs and 0.20–1.93 μA/W in the case of MoS_2 PDs. For TiS_3–MoS_2 PDs, these values are measured in the range of 0.08 to 0.19 mA/W. Accordingly, MoS_2 has the lowest photoresponsivity and TiS_3 possess the highest photoresponsivity. However, both photoresponsivity and photocurrent of TiS_3–MoS_2 PDs are considerable compared to the MoS_2 PD. Moreover, a similar trend is observed in the order of magnitude of all calculated R in these PDs. Figure 6b shows the photoresponsivity of all three devices in terms of different laser wavelengths at the
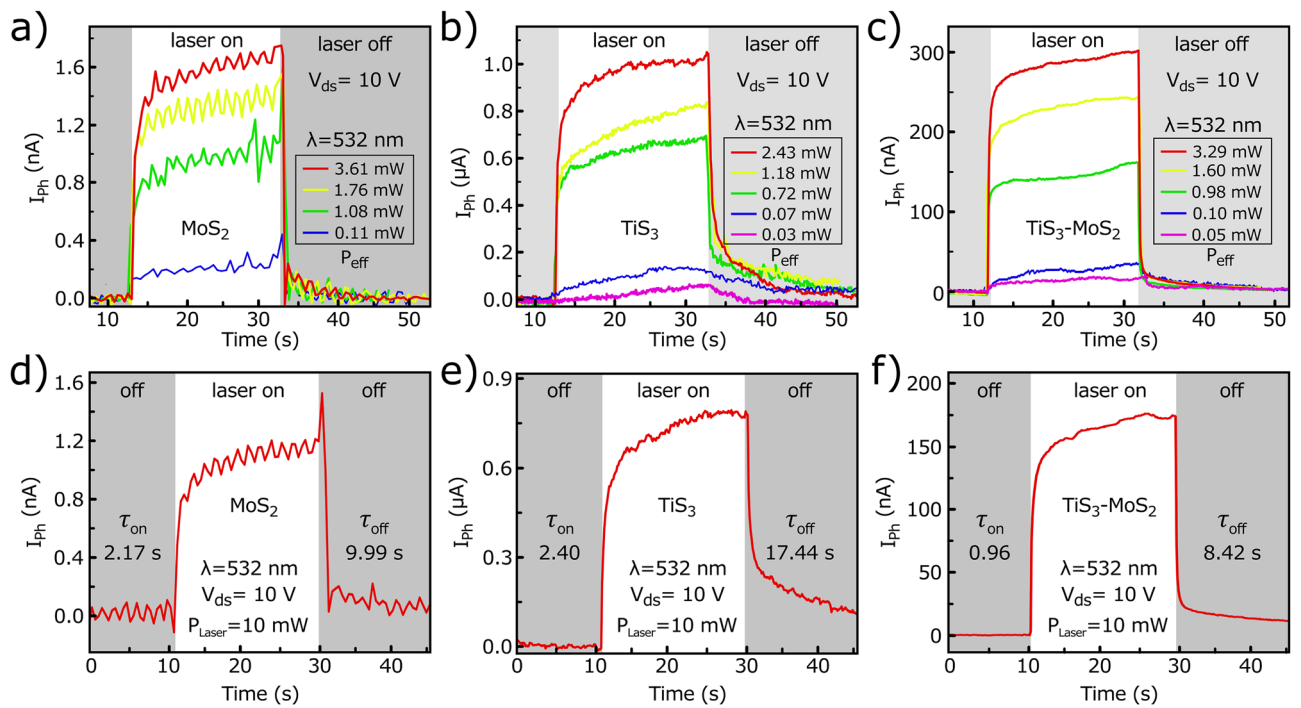
Figure 5. The measured Photocurrent as a function of laser intensities for (**a**) MoS$_2$, (**b**) TiS$_3$, and (**c**) TiS$_3$-MoS$_2$ PDs under 532 nm laser illumination at a constant voltage of 10 V. Time trace measurement of (**d**) MoS$_2$, (**e**) TiS$_3$, and (**f**) TiS$_3$-MoS$_2$ PDs under 532 nm laser illumination at an applied voltage of 10 V and laser intensity of 10 mW. The corresponding P$_{eff}$ was calculated to be 1.53 mW, 1.03 mW, and 1.39 mW for panels (**d**) to (**f**), respectively.

same power of 15 mW and supply voltage of 10 V. All three PDs have a broad response within the range of 400 to 800 nm. The photoresponsivity of the TiS$_3$ PDs are one order of magnitude greater than that of the TiS$_3$–MoS$_2$ PDs and two orders greater than that of the MoS$_2$ PDs. Figure 6c compares the measured I$_{on}$/I$_{off}$ ratio and dark current of all three PDs under 532 nm laser irradiation. The error line shows the deviation of the values obtained for the same PDs. The on–off ratio (I$_{on}$/I$_{off}$) is usually used to describe the signal-to-noise ratio[28]. According to Fig. 6c, the values of 1.35, 0.17, and 1.82 are obtained for MoS$_2$, TiS$_3$, and TiS$_3$–MoS$_2$ PDs, respectively. Based on them, the highest signal-to-noise ratio is related to the TiS$_3$–MoS$_2$ PDs. Interestingly, the dark currents are lowest in MoS$_2$ (~ 1.2 nA) and highest in TiS$_3$ (~ 6.0 μA). Since the light detection mechanism is based on the change of drain current in these PDs, less dark current provides better performance in light detection as will be discussed below[29]. Another important parameters are the rise and fall times which are presented in Fig. 6d. Accordingly, the TiS$_3$-MoS$_2$ PD has the fastest response time to laser radiation than the other two PDs. Figure 6e shows the energy band diagram of the TiS$_3$–MoS$_2$ heterostructure and its corresponding photodetection mechanism. TiS$_3$ is an n-type semiconductor with an energy band gap of 1.1 eV and MoS$_2$ is also an n-type semiconductor with an energy band gap in the range of 1.2–1.8 eV[30,31]. Here, the energy band gap of bulk MoS$_2$ is considered because most layers are thick, although the deposited film can contain single and few layers of MoS$_2$. The electron affinities of MoS$_2$ and TiS$_3$ are around 4 and 4.7 eV, respectively, and hence the conduction band of TiS$_3$ is located of MoS$_2$, forming an n–n$^+$ heterostructure[32,33]. In the MoS$_2$ film under laser irradiation, electron–hole pairs are generated and the photogenerated electrons enter into the TiS$_3$ due to its lower conduction band which prevents electrons from recombination with the holes. Moreover, the valence band of MoS$_2$ is located higher than that of TiS$_3$ resulting in transferring of minority holes from TiS$_3$ into MoS$_2$. Hence, the recombination rate of the carriers is decreased in the heterostructure. Such charge separation in the heterostructure is responsible for faster response time, and improved photoresponsivity of the heterostructure compared with individual MoS$_2$ PDs.

In order to investigate the effect of thicknesses, the performance of the three hybrid PDs was evaluated with three different TiS$_3$ thicknesses. In this regard, thicknesses of ~ 2, ~ 10 and ~ 20 μm were prepared where dark current and photoresponsivity of the PDs were measured as reported in the Fig. S7. Based on the result, as the thickness of TiS$_3$ increases, the dark current increases but the photoresponsivity decreases. Less thickness of TiS$_3$ leads to more changes in electrical current, which can be due to non-uniformity of the deposited film. Moreover, as the thickness increases, the upper layers are more involved in light absorption and the lower layers play a lesser role in the photogenerated carriers. Therefore, the ratio of photogenerated to non-photogenerated carriers decreases, which leads to a decrease in photoresponsivity. As can be seen, the thickness of ~ 10 μm generally shows better performance compared to less and more thicknesses.

To evaluate the air stability of the PDs, the performance of the fresh devices was also investigated after two weeks based on the measured photocurrent. Based on the Fig. S8, it can be seen that after two weeks of device life, the performance of the PDs is very close to the fresh states, which show their high environmental stability.
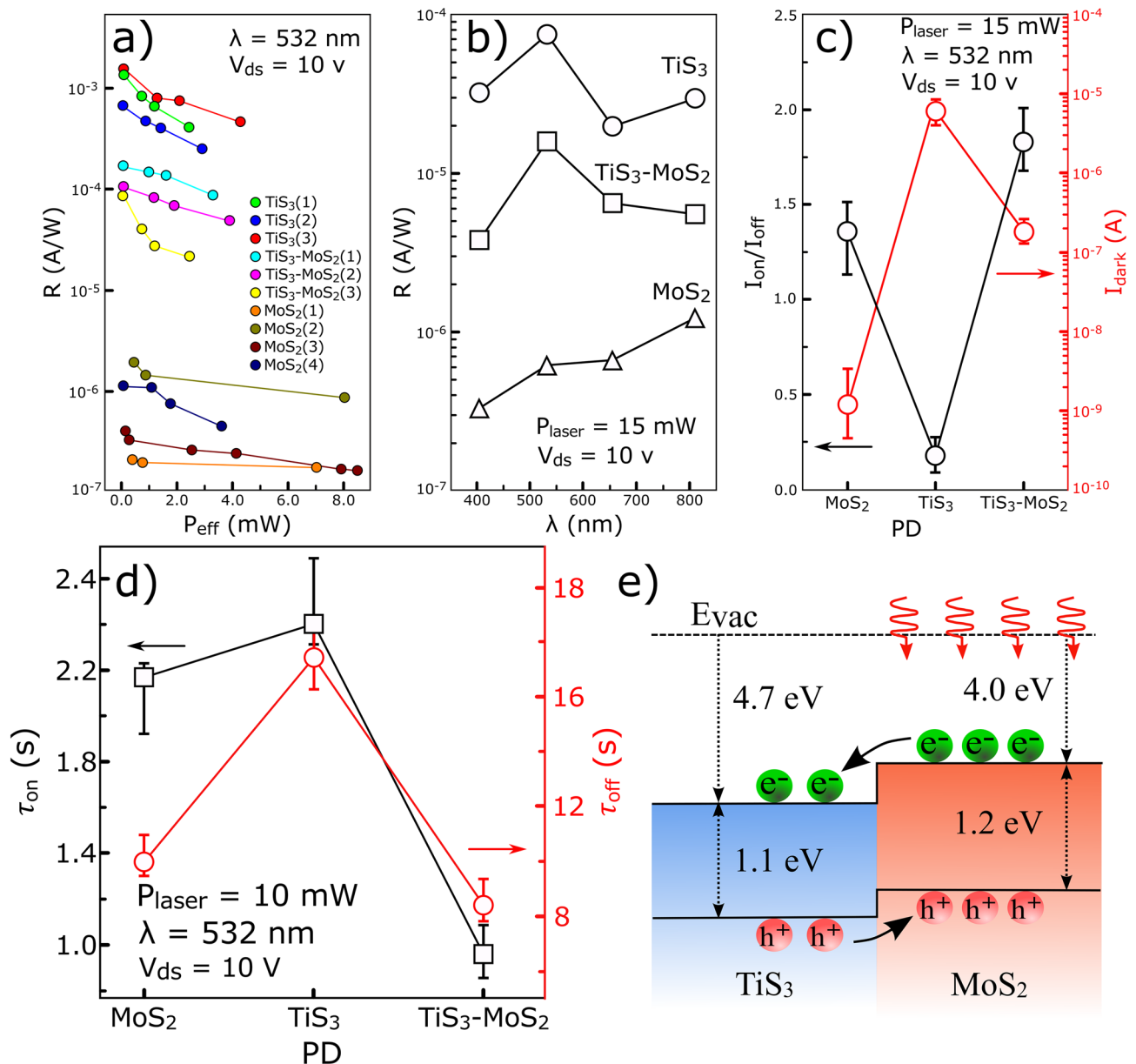
Figure 6. Comparison of (**a**) photoresponsivity as a function of the incident power for several fabricated PDs at an applied voltage of 10 V under a laser wavelength of 532 nm, (**b**) the photoresponsivity of fabricated PDs under various laser wavelengths at an applied voltage of 10 V, (**c**) I_{on}/I_{off} and dark current, (**d**) rise and fall times of the MoS_2, TiS_3, TiS_3-MoS_2 PDs at a constant voltage of 10 V, and (**e**) Energy band diagram and detection mechanism in the TiS_3-MoS_2 heterojunction.

Since the substrate is made of paper, the performance of the introduced PDs was thoroughly investigated under applied strain. For this purpose, a homemade setup was fabricated to apply strain to the substrates as shown in Fig. S9. This setup includes a cage covered with aluminum foil to act as a Faraday cage. The sample is fixed to a motor shaft through a hook to provide upward and downward strains by moving in a clockwise or counter-clockwise direction. The strain applied to the PDs was calculated according to $\varepsilon = t/2R$ equation, where t is the thickness of the substrate and r is the radius of bending curvature[34]. Figure S10 presents the applied strains in the PDs, which are performed in the range of -0.54% to $+0.54\%$˚. As can be seen, at strains larger than $\pm 0.33\%$, a significant bending is occurred in the substrates.

Figure 7a and b show the schematic of applying the upward (uniaxial tensile) and downward (compression) strains in the PDs under exposing to 532 nm laser illuminations, respectively. Panels (c), (d), and (e) of Fig. 7 compare the I_{ds}-V curves of the MoS_2, TiS_3, and TiS_3–MoS_2 PDs in the flat state and under negative and positive strains, respectively. For the MoS_2 sample, it is observed that the drain current in the flat state almost remains the same as under different applied strains without any significant change. The flexible and soft structure of MoS_2 is the main reason for this behavior[35]. Moreover, due to the polycrystalline structure of MoS_2 flakes and their different thicknesses, the applied strain has a negligible effect on the channel current[36]. In the case of TiS_3, it is
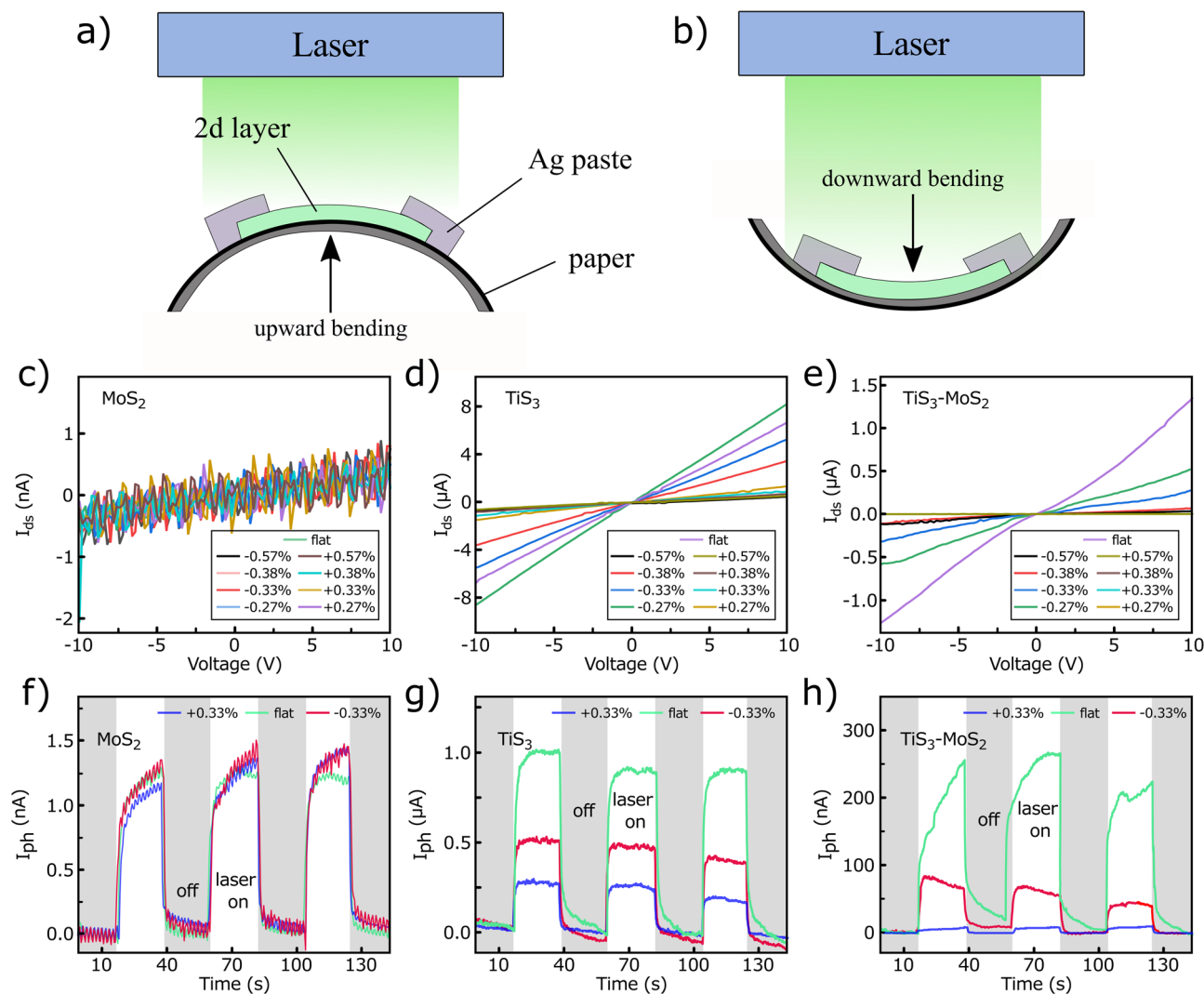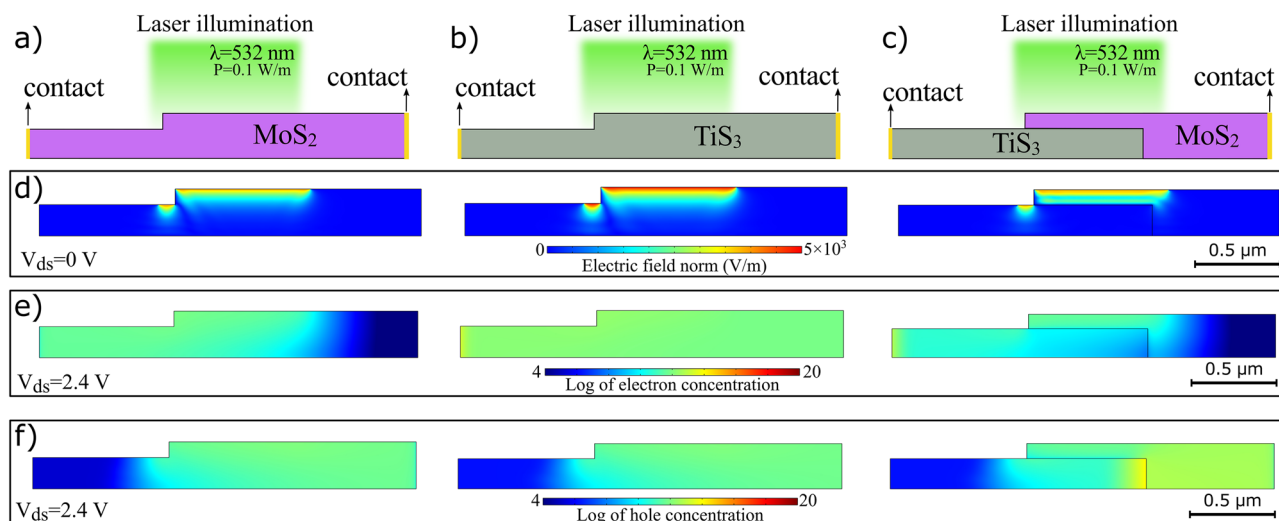
Figure 7. Schematic illustrations of (**a**) upward and (**b**) downward applied strains at the PDs under laser illuminations. I_{ds}-V curves of the (**c**) MoS_2, (**d**) TiS_3, and (**e**) TiS_3-MoS_2 PDs under different applied strains. Photocurrent switching performance of the (**f**) MoS_2, (**g**) TiS_3, and (**h**) TiS_3-MoS_2 PDs in flat state and at applied strains of ± 0.33% under 532 nm laser illumination at a bias voltage of 10 V.

found that the I_{ds} decreases after applying downward strains, but a more significant decrease is observed in the upward strains. Moreover, after upward strain, by returning the TiS_3 to its flat position, current does not return to its original value of before any strain. The structure of the needle-like TiS_3 flake is more fragile than that of MoS_2, and bending can break the contact between TiS_3 and Ag paste, affecting the conductivity[37]. As a result, even after the sample has returned to the flat state, the current dramatically suffers from decline. In detail, by applying + 0.57% strain, a relative change of drain current $|\Delta I/I_{flat}|$ is measured to be ~ 88% compared to the flat state, which indicates the high fragility of the TiS_3 flakes within the channel. A similar trend is observed in the TiS_3–MoS_2 PD, but with a more noticeable decrease after positive strains, which could be due to the separation of the two films at the interface and the reduction of the electric field in the channel.

Figure 7f–h show the photocurrent characteristics of all PDs under 532 nm laser irradiation at a drain voltage of 10 V and an incident power of 15 mW. For MoS_2 PD, the photocurrent is well switched under negative and positive strains of 0.33% similar to the flat state. The lack of change in the photocurrent as well as the slight change in the drain current under the applied strain indicate that the tensile and compressive strains have no effect on the band gap, density of state of carriers, and barrier height at the contacts of the MoS_2 PDs. This is probably due to the presence of MoS_2 flakes of different thicknesses and their polycrystalline nature which minimize the effect of strain[36]. In the case of TiS_3, the photocurrent is about 1.00 μA in the flat state, which is reduced to 0.50 and 0.25 μA in the applied strains of − 0.33 and + 0.33%. This reduction in photocurrent is not due to a change in the energy gap or piezoresistive effect, but rather to the breaking of the needle-like TiS_3 flakes in the channel, which leads to their less contribution in the drain current and generation of photocarriers. For TiS_3-MoS_2, the current is about 250 nA in the flat state, which is reduced to ~ 70 and ~ 10 nA by applying positive and negative strains. As discussed, the brittle structure of TiS_3 as well as the separation of the two films at the junction, especially at a strain of + 0.33% are the main factors in the TiS_3–MoS_2 PD performance drop under applied strains.

Figure 8. Schematic illustrations of device geometries for (**a**) MoS$_2$ (**b**) TiS$_3$ and (**c**) TiS$_3$-MoS$_2$ heterostructure, (**d**) exposed surface of the devices and light-induced electric field, (**e**) electron and (**f**) hole concentrations in a logarithmic scale for the three devices.

Paper-based PDs	V_{ds} (V)	λ (nm)	R (μA/W)	Ref
Te-TiO$_2$	0	400	30	[38]
ZnS-MoS$_2$	1	554	18	[39]
MoTe$_2$	1	532	1.1	[40]
MoSe$_2$	1	532	0.2	
WS$_2$	1	532	0.06	
MoS$_2$	1	532	0.02	
MoS$_2$	20	532	1.1	[14]
MoS$_2$	10	532	1.2	This work
TiS$_3$	10	532	1600	
TiS$_3$-MoS$_2$	10	532	170	

Table 1. Comparison of the performance of introduced paper-based PDs with other PDs based on different 2D materials.

Numerical simulation is employed to present further insight about the physics of light-induced generation-recombination processes for charged carriers in these devices. We used the model to calculate the photocurrent of the devices in response to the incident light under various biasing conditions. Details of the simulation can be found in the supporting information section. Panels (a) to (c) of Fig. 8 depict the schematic of the devices consisting MoS$_2$, TiS$_3$ and heterostructure with stacked layers of both materials. Overlapped part in the heterostructure device was exposed to the incident light with the wavelength of 532 nm. Stray electromagnetic field due to unintentional exposure is also took into the account. Corresponding light-induced electric field can be seen in Fig. 8d for all devices due to laser exposure. Vertical electric field was established by applying a voltage difference between the two terminals at both ends, where contacts are located. Figure 8e–f show the electron and hole concentrations under this biasing condition in a logarithmic scale, respectively. As can be seen, the distribution of electrons and holes in the two structures of MoS$_2$ and TiS$_3$ is almost uniform, but in the TiS$_3$–MoS$_2$ device, the band offset accelerates the separation of electrons and holes and causes a non-uniform distribution of carriers at the two-layer boundary. These results indicate that the formed n–n + heterostructure can more efficiently separate the charge and confirms its superior optoelectronic performance compared with the individual MoS$_2$ case.

At various light intensities, I–V characteristic curves has been simulated for MoS$_2$, TiS$_3$, and TiS$_3$–MoS$_2$ photodetectors. The obtained curves for drain currents are consistent with the measurements as illustrated in Fig. S11a–c. Relative differences between the amplitude of photocurrent is in all devices is in total agreement with the experiments where TiS$_3$ and MoS$_2$ PDs have higher and lower photocurrents, respect to the hybrid structure under identical biasing and light exposure conditions.

Table 1 compares the performance of the introduced PDs with some other reported paper-based PDs. According to it, most of them have a photoresponsivity in the range of a few μA/W. In the case of MoS$_2$, it is observed that our introduced PD has a slightly higher photoresponsivity than the others. The TiS$_3$ PD shows a much higher photoresponsivity (in the range of mA/W), which has a significant improvement in performance compared to other reported PDs. However, it shows a larger dark current and a smaller on/off ratio than MoS$_2$ PDs which can

9

limit its optical detection performance. Finally, the photoresponsivity of the TiS_3–MoS_2 heterostructure shows a significant improvement, which indicates its superiority over other works.

Conclusions. The two-dimensional (2D) layered family of transition metals chalcogenides shows high potential as photodetectors because they not only interact effectively with light but also provide high carrier transport properties. In this report, a very simple, fast and promising clean method is introduced to fabricate the paper-based photodetectors using MoS_2, TiS_3 and their integration. The all introduced photodetectors show remarkable photoresponsivities in the range of 405 to 810 nm. In the case of TiS_3–MoS_2 heterostructure, it associates with fast response time and large on–off ratio compared to individual MoS_2 and TiS_3 photodetectors. The numerical simulation results are consistent with the experimental results and confirm the superiority of the hybrid structure over the two other PDs. Moreover, the bending results of the photodetectors indicate that in applied strains smaller than $\pm 0.33\%$, these devices still show acceptable performance.

Methods

Material. Naturally occurring molybdenite crystal, from Wolfram Camp Mine, Queensland, Australia, were used. Silver paste was purchased from Dycotec Materials, UK DM-SIP-3060S. Ordinary papers (CopiMax, Thailand) were used as substrates.

Growth of TiS_3 microcrystals. TiS_3 microcrystals were synthesized by a solid–gas reaction of titanium powder through direct sulfurization. In detail, titanium powder (Goodfellow, > 99% purity) and sulfur powder (Merck, > 99.9% purity) were vacuum sealed in an ampule and heated up to 500 °C for 20 h. Then, the ampule was cooled down to room temperature and grown microcrystals were collected.

Fabrication of MoS_2 (TiS_3) paper-based photodetector. First, a piece of paper with 2×6 cm^2 dimensions was cut and attached on a slide glass using adhesive tape. A shadow mask (a 1×6 mm^2 rectangular window) was then opened in the center of the paper with adhesive tape. A piece of bulk MoS_2 (or TiS_3) was rubbed several times along the length and width of the open-window reign. After deposition of a homogeneous layer of MoS_2 (TiS_3), the mask was removed from the paper. Silver paste was then placed on the both sides of the deposited film, and two pieces of soft copper wire were mounted on the paste and kept at room temperature for 24 h for improving the adhesion. Then, the dried silver paste was covered with epoxy glue for strengthening and achieving higher mechanical stability. The photograph of the fabrication steps of MoS_2 and TiS_3 PDs are presented in the supporting file.

Fabrication of TiS_3-MoS_2 paper-based photodetector. First, a piece of paper with a dimension of 2×6 cm^2 was cut and attached to a slide glass. A rectangular shadow mask (mask 1) was opened by the adhesive tape in the center of the paper. With the use of another mask (mask 2), this part was divided into two sections with dimensions of 1×4 mm^2 (for TiS_3 deposition) and 1×2 mm^2 (for MoS_2 deposition). A piece of bulk TiS_3 was rubbed several times in the open-window region. Then, mask 2 was removed from the paper and MoS_2 crystal was finger-rubbed several times on the 1×2 mm^2 part of the bare paper and 1×1 mm^2 part of the deposited TiS_3. Thus, the center of the sample (device) with dimensions of 1×1 mm^2 was a film composed of TiS_3 and MoS_2, in which TiS_3 was placed beneath the MoS_2 film. After removing mask 1 from the paper, a homogeneous film composed of TiS_3, MoS_2 and, TiS_3–MoS_2 with dimensions of 1×3, 1×1, and 1×1 mm^2 can be achieved, respectively. Similar to previous PDs, copper wires were added to both sides of the film. The TiS_3-MoS_2 PD is ready for testing.

Characterizations. SEM images and EDX analyses were taken by TESCAN MIRA 3 and EDX (Energy-dispersive X-ray) systems. Crystalline structure was identified by using a Panalytical X`Pert Pro X-ray diffractometer at glancing angle configuration (incident angle of 1.7°) with CuKα radiation. Raman spectra of the transferred flakes were measured by Avantes (AVASPEC-ULS3648-RS) system under 532 nm laser illumination. Electrical measurements were carried out by a Keithley 2450 source meter. Optical measurements were done under different laser excitations including 405, 532, 655, and 810 nm at room temperature in air ambient. Bending tests were performed with a homemade setup capable of applying both upward and strains.

Data availability
The datasets generated and/or analysed during the current study are not publicly available due to privacy or ethical restrictions. But are available from the corresponding author on reasonable request.

References

1. Shi, Q. *et al.* Progress in wearable electronics/photonics—Moving toward the era of artificial intelligence and internet of things. *InfoMat* **2**, 1131–1162. https://doi.org/10.1002/inf2.12122 (2020).
2. Zhuo, L. *et al.* Cost-effective silver nano-ink for inkjet printing in application of flexible electronic devices. *Chem. Phys. Lett.* **757**, 137904. https://doi.org/10.1016/j.cplett.2020.137904 (2020).
3. Devi, R. *et al.* A low-cost paper-based flexible energy storage device using a conducting polymer nanocomposite. *New J. Chem.* **44**, 13446–13457. https://doi.org/10.1039/D0NJ02158J (2020).

4. Gao, L. *et al.* All paper-based flexible and wearable piezoresistive pressure sensor. *ACS Appl. Mater. Interfaces* **11**, 25034–25042. https://doi.org/10.1021/acsami.9b07465 (2019).
5. Sala de Medeiros, M., Chanci, D. & Martinez, R. V. Moisture-insensitive, self-powered paper-based flexible electronics. *Nano Energy* **78**, 105301. https://doi.org/10.1016/j.nanoen.2020.105301 (2020).
6. Dong, T., Simões, J. & Yang, Z. Flexible photodetector based on 2D materials: Processing, architectures, and applications. *Adv. Mater. Interfaces* **7**, 1901657. https://doi.org/10.1002/admi.201901657 (2020).
7. Cheng, Z. *et al.* 2D materials enabled next-generation integrated optoelectronics: From fabrication to applications. *Adv. Sci.* **8**, 2003834. https://doi.org/10.1002/advs.202003834 (2021).
8. Wang, B. *et al.* Broadband photodetectors based on 2D group IVA metal chalcogenides semiconductors. *Appl. Mater. Today* **15**, 115–138. https://doi.org/10.1016/j.apmt.2018.12.010 (2019).
9. Pataniya, P. M., Patel, V. & Sumesh, C. K. MoS2/WSe2 nanohybrids for flexible paper-based photodetectors. *Nanotechnology* **32**, 315709. https://doi.org/10.1088/1361-6528/abf77a (2021).
10. Sahatiya, P., Kadu, A., Gupta, H., Thanga Gomathi, P. & Badhulika, S. Flexible, disposable cellulose-paper-based MoS2/Cu2S hybrid for wireless environmental monitoring and multifunctional sensing of chemical stimuli. *ACS Appl. Mater. Interfaces* **10**, 9048–9059. https://doi.org/10.1021/acsami.8b00245 (2018).
11. Selamneni, V., Raghavan, H., Hazra, A. & Sahatiya, P. MoS2/paper decorated with metal nanoparticles (Au, Pt, and Pd) based plasmonic-enhanced broadband (Visible-NIR) flexible photodetectors. *Adv. Mater. Interfaces* **8**, 2001988. https://doi.org/10.1002/admi.202001988 (2021).
12. Sahatiya, P., Jones, S. S. & Badhulika, S. 2D MoS2–carbon quantum dot hybrid based large area, flexible UV–vis–NIR photodetector on paper substrate. *Appl. Mater. Today* **10**, 106–114. https://doi.org/10.1016/j.apmt.2017.12.013 (2018).
13. Cordeiro, N. J. A. *et al.* Fast and low-cost synthesis of MoS2 nanostructures on paper substrates for near-infrared photodetectors. *Appl. Sci.* **11**, 1234 (2021).
14. Mazaheri, A., Lee, M., van der Zant, H. S. J., Frisenda, R. & Castellanos-Gomez, A. MoS2-on-paper optoelectronics: Drawing photodetectors with van der Waals semiconductors beyond graphite. *Nanoscale* **12**, 19068–19074. https://doi.org/10.1039/D0NR02268C (2020).
15. Talib, M., Tabassum, R., Abid Islam, S. S. & Mishra, P. Improvements in the Performance of a Visible–NIR Photodetector Using Horizontally Aligned TiS3 Nanoribbons. *ACS Omega* **4**, 6180–6191. https://doi.org/10.1021/acsomega.8b03067 (2019).
16. Baraghani, S. *et al.* Printed electronic devices with inks of TiS3 quasi-one-dimensional van der waals material. *ACS Appl. Mater. Interfaces* **13**, 47033–47042. https://doi.org/10.1021/acsami.1c12948 (2021).
17. Ghasemi, F. & Hassanpour Amiri, M. Facile in situ fabrication of rGO/MoS2 heterostructure decorated with gold nanoparticles with enhanced photoelectrochemical performance. *Appl. Surf. Sci.* **570**, 151228. https://doi.org/10.1016/j.apsusc.2021.151228 (2021).
18. Ghasemi, F. *et al.* tunable photodetectors via in situ thermal conversion of TiS3 to TiO2. *Nanomaterials* **10**, 711 (2020).
19. Frisenda, R. *et al.* Dielectrophoretic assembly of liquid-phase-exfoliated TiS3 nanoribbons for photodetecting applications. *Chem. Commun.* **53**, 6164–6167. https://doi.org/10.1039/C7CC01845B (2017).
20. Ghasemi, F. Vertically aligned carbon nanotubes, MoS2–rGo based optoelectronic hybrids for NO2 gas sensing. *Sci. Rep.* **10**, 11306. https://doi.org/10.1038/s41598-020-68388-2 (2020).
21. Liang, Q. *et al.* High-performance, room temperature, ultra-broadband photodetectors based on air-stable PdSe2. *Adv. Mater.* **31**, 1807609. https://doi.org/10.1002/adma.201807609 (2019).
22. Island, J. O. *et al.* Ultrahigh photoresponse of few-layer TiS3 nanoribbon transistors. *Adv. Opt. Mater.* **2**, 641–645. https://doi.org/10.1002/adom.201400043 (2014).
23. Xiang, H. *et al.* Long-term stable near-infrared–short-wave-infrared photodetector driven by the photothermal effect of polypyrrole nanostructures. *ACS Appl. Mater. Interfaces* **13**, 45957–45965. https://doi.org/10.1021/acsami.1c11674 (2021).
24. Li, F., Tao, R., Cao, B., Yang, L. & Wang, Z. Manipulating the light-matter interaction of PtS/MoS2 p–n junctions for high performance broadband photodetection. *Adv. Func. Mater.* **31**, 2104367. https://doi.org/10.1002/adfm.202104367 (2021).
25. Ma, Z., Yang, L., Liu, L., Wang, S. & Peng, L.-M. Silicon-waveguide-integrated carbon nanotube optoelectronic system on a single chip. *ACS Nano* **14**, 7191–7199. https://doi.org/10.1021/acsnano.0c02139 (2020).
26. Gong, F. *et al.* Visible to near-infrared photodetectors based on MoS2 vertical Schottky junctions. *Nanotechnology* **28**, 484002. https://doi.org/10.1088/1361-6528/aa9172 (2017).
27. Taffelli, A., Dirè, S., Quaranta, A. & Pancheri, L. MoS2 based photodetectors: A review. *Sensors* **21**, 2758 (2021).
28. Yu, M. *et al.* High-performance photodetector based on sol–gel epitaxially grown α/β Ga2O3 thin films. *Mater. Today Commun.* **25**, 101532. https://doi.org/10.1016/j.mtcomm.2020.101532 (2020).
29. Long, M., Wang, P., Fang, H. & Hu, W. Progress, challenges, and opportunities for 2D material based photodetectors. *Adv. Func. Mater.* **29**, 1803807. https://doi.org/10.1002/adfm.201803807 (2019).
30. Chaves, A. *et al.* Bandgap engineering of two-dimensional semiconductor materials. *npj 2D Mater. Appl.* **4**, 29. https://doi.org/10.1038/s41699-020-00162-4 (2020).
31. Ghasemi, F. & Mohajerzadeh, S. Sequential solvent exchange method for controlled exfoliation of MoS2 suitable for phototransistor fabrication. *ACS Appl. Mater. Interfaces* **8**, 31179–31191. https://doi.org/10.1021/acsami.6b07211 (2016).
32. Agarwal, A. *et al.* Anomalous isoelectronic chalcogen rejection in 2D anisotropic vdW TiS3(1−x)Se3x trichalcogenides. *Nanoscale* **10**, 15654–15660. https://doi.org/10.1039/C8NR04274H (2018).
33. Ghasemi, F., Abdollahi, A. & Mohajerzadeh, S. Controlled plasma thinning of bulk MoS2 flakes for photodetector fabrication. *ACS Omega* **4**, 19693–19704. https://doi.org/10.1021/acsomega.9b02367 (2019).
34. Roldán, R., Castellanos-Gomez, A., Cappelluti, E. & Guinea, F. Strain engineering in semiconducting two-dimensional crystals. *J. Phys. Condens. Matter* **27**, 313201. https://doi.org/10.1088/0953-8984/27/31/313201 (2015).
35. Kang, M.-A. *et al.* Fabrication of flexible optoelectronic devices based on MoS2/graphene hybrid patterns by a soft lithographic patterning method. *Carbon* **116**, 167–173. https://doi.org/10.1016/j.carbon.2017.02.001 (2017).
36. Tsai, M.-Y. *et al.* Flexible MoS2 field-effect transistors for gate-tunable piezoresistive strain sensors. *ACS Appl. Mater. Interfaces* **7**, 12850–12855. https://doi.org/10.1021/acsami.5b02336 (2015).
37. Lou, Z. & Shen, G. Flexible photodetectors based on 1D inorganic nanostructures. *Adv. Sci.* **3**, 1500287. https://doi.org/10.1002/advs.201500287 (2016).
38. Zhang, Y. *et al.* Low-cost writing method for self-powered paper-based UV photodetectors utilizing Te/TiO2 and Te/ZnO heterojunctions. *Nanoscale Horiz.* **4**, 452–456. https://doi.org/10.1039/C8NH00401C (2019).
39. Gomathi, P. T., Sahatiya, P. & Badhulika, S. Large-area, flexible broadband photodetector based on ZnS–MoS2 hybrid on paper substrate. *Adv. Func. Mater.* **27**, 1701611. https://doi.org/10.1002/adfm.201701611 (2017).
40. McManus, D. *et al.* Photocurrent study of all-printed photodetectors on paper made of different transition metal dichalcogenide nanosheets. *Flex. Print. Electron.* **3**, 034005. https://doi.org/10.1088/2058-8585/aaddb5 (2018).

Acknowledgements

Author contributions

E.M. done the experimental part.M.H.A. done the simulation part.A.S. provided lab equipment.R.F. provided calibrated photodiodes.E.F grown TiS3 microcrystals.J.R.A grown TiS3 microcrystals.I.J.F provided TiS3 micro-crystals, and discussed about the results.A.C provided MoS2 crystals, and discussed about the results.F.G wrote the manuscript, prepared the Figures and analyzed the data.All authors reviewed the manuscript.

Competing interests

The authors declare no competing interests.

Additional information

Supplementary Information The online version contains supplementary material available at https://doi.org/10.1038/s41598-022-16834-8.

Correspondence and requests for materials should be addressed to F.G.

Reprints and permissions information is available at www.nature.com/reprints.

Publisher's note Springer Nature remains neutral with regard to jurisdictional claims in published maps and institutional affiliations.